Calculating and fitting morphology-dependent resonances of a spherical particle with a concentric spherical shell

August 19, 2019

Benjamin Vennes and Thomas C. Preston*

Department of Atmospheric and Oceanic Sciences

and Department of Chemistry,

McGill University, 805 Sherbrooke Street West, Montreal, QC, Canada H3A 0B9

submitted to the Journal of the Optical Society of America A

11 Figures, 3 Appendices, and 22 manuscript pages

* Thomas C. Preston

e-mail: thomas.preston@mcgill.ca

Abstract

Determining the size and composition of core-shell particles using morphology-dependent resonances (MDRs) is a computationally intensive problem due to the large parameter space that needs to be searched during the fitting process. Very often it is not even practical to consider a reasonable range of physical parameters due to time constraints, leading to restrictive assumptions concerning the system being studied. The lengthy computational time is so limiting that there has, to date, been no systematic study of fitting measured MDRs for core-shell particles. In this work, we address the issue of fitting speed by developing an algorithm that (i) reduces the multi-dimensional grid search to a one-dimensional search using a least squares method and (ii) implements a new method for calculating MDRs that is much faster than previous methods. With the program presented here, we are able to provide a comprehensive analysis of best-fits for core-shell MDRs across a large range of physically relevant scenarios using noise levels typical for conventional spectroscopic experiments. For many cases it is found that excellent fits can be quickly determined. However, there are also some surprising situations where accurate best-fits are not possible (e.g. if only one mode order is present in the measured MDR set).

OCIS Codes: (140.4780) Optical resonators; (260.2030) Dispersion; (290.3030) Index measurements; (290.4020) Mie theory

1 Introduction

Morphology-dependent resonances (MDRs) are often observed in the optical spectra of single, micron-sized spherical particles. Sharp MDRs occur when a dielectric particle behaves as a high-quality factor cavity that supports resonant electromagnetic modes at optical frequencies.[1–3] These sharp MDRs are also referred to as whispering gallery modes and can be seen to have strong internal electromagnetic fields at the interior interface of the particle, which can be attributed to total internal reflection of the incident light inside the particle.[3–5] Spectra containing MDRs can be collected using both elastic and inelastic light scattering techniques such as broadband light scattering,[6–12] cavity-enhanced fluorescence spectroscopy,[13–18] and cavity-enhanced Raman spectroscopy.[7,12,19–22]

For spherical particles with a uniform composition, measured MDR positions can quickly be fitted using a resonance condition from Mie theory, allowing for the simultaneous retrieval of particle size and refractive index.[16,23,24] Beyond homogeneous spheres, using observed MDRs to accurately characterize particles presents an enormous challenge. First, it will be inadequate to describe the object using only a radius and a single wavelength-dependent refractive index. This will lead to an increase in the dimensions of the physical parameter space that needs to be searched. Second, for an object with an arbitrary shape and refractive index profile, a characteristic equation for the MDR positions will likely not exist, leading to much more laborious calculations than are necessary with MDRs determined using Mie theory. For instance, light scattering for a spherical particle with a non-uniform refractive profile can be calculated by approximating the refractive index profile using a multilayered sphere.[25,26] Determining the locations of MDRs from such calculations, while possible,[27,28] is tedious and time consuming.

Fig. 1 shows a particle that consists of a spherical core with a concentric spherical shell. It can be seen that there will be twice as many parameters to fit when compared to a homogeneous sphere (assuming all refractive indices have the same number of terms). A resonance condition for transverse electric (TE) and transverse magnetic (TM) modes can be found using the denominators of the scattering coefficients that have been given for the solution to the problem of the scattering of a plane wave for a sphere with a concentric spherical shell.[29] The behavior of MDRs for this type of core-shell particle have been investigated previously.[27,30–32] Resonances for both spherical and core-shell particles are found by solving a transcendental equation. For the homogeneous sphere there is an approximate explicit formula for the MDR positions[33] and this is tremendously useful as an initial guess in solving the exact resonance condition.[23,24] While approximate explicit formulas do exist for the core-shell particle, they are only valid under fairly restrictive conditions (thin shell or small refractive index difference between the core and shell).[34,35] The core-shell equation can still be reliably solved for a given mode assignment, however, it can be a very computationally intensive task.

The sensitivity of MDRs to both changes in size and refractive index of the core and shell can potentially allow a core-shell particle to be studied with high precision and is the primary motivator for their applied use. Utilizing core-shell MDRs has applications that include probing thin coatings on droplets,[36,37] investigating liquid-liquid phase separation in aerosol particles,[38–41] and tracking penetrant uptake in microspheres.[27,28,35] Liquid-liquid phase separation, in particular, has received considerable attention from the atmospheric science community as it has been proposed that the lower surface tension of a phase separated particle when compared to a homogeneously mixed particle will result in an enhancement of cloud condensation nuclei activity.[42–44]

The aim of this work is two-fold: (i) Develop a fast yet robust fitting algorithm that can be used to characterize core-shell particles using measured MDR positions, and (ii) Study the accuracy of the best-fits. The first objective is met by formulating and solving the fitting problem using the method of least squares (Section 2). Unlike previously implemented grid search based algorithms, the least squares approach developed here is much faster as, once the mode assignment is known, the N parameters of best-fit can be found by solving N linear equations as oppose to performing a grid search across a N-dimensional hypersurface (although for the core-shell particle a one-dimensional grid search is still necessary). Further speed improvements are presented in Section 3, where a new method for calculating core-shell MDRs is demonstrated to be much faster than previous methods in many situations. In Section 4, we evaluate the accuracy of the fitting algorithm using a wide range of synthetic data sets. This analysis reveals that excellent best-fits are possible for many physically plausible cases but that there are also unexpected issues with certain MDR sets.

2 Formulation and solution to the least squares problem

Given a set of J resonance positions measured at the wavenumbers ν_j, our objective is to determine a set of calculated resonances, ν_j^c, that minimizes the sum of squared differences:

$$S = \sum_{j=1}^{J} \left(\nu_j - \nu_j^c\right)^2. \tag{1}$$

For a particle consisting of a spherical core with a concentric spherical shell (a core-shell particle), the parameters that are used to calculate each ν_j^c are the wavenumber-dependent refractive index of the core, m_{1j}, the wavenumber-dependent refractive index of the shell, m_{2j}, the core radius, a_1, and the shell radius a_2 (Fig. 1). The refractive indices of the core and shell are relative to the medium that surrounds the particle.

Eq. 1 can be rewritten in terms of the outer radius and the resonant size parameters of the shell, x_{2j}, using the relationship $x_{2j} = 2\pi a_2 \nu_j^c$. This yields

$$S = \sum_{j=1}^{J} \left(\nu_j - \frac{x_{2j}}{2\pi a_2}\right)^2. \tag{2}$$

Each jth resonant size parameter depends on m_{1j}, m_{2j}, and the ratio between the radius of the core and the radius of the shell, $r = a_1/a_2$. If r is fixed at r_0, the functions x_{2j} can be expanded using a first-order Taylor series around the points $m_{0,1j}$ and $m_{0,2j}$ as

$$x_{2j}(m_{1j}, m_{2j}, r_0) = x_{2j}(m_{0,1j}, m_{0,2j}, r_0) + (m_{1j} - m_{0,1j})\frac{\partial x_{2j}}{\partial m_{1j}} + (m_{2j} - m_{0,2j})\frac{\partial x_{2j}}{\partial m_{2j}}. \tag{3}$$

For brevity Eq. 3 will be written as

$$x_{2j}(m_{1j}, m_{2j}, r_0) = p_j m_{1j} + q_j m_{2j} + b_j, \tag{4}$$

where p_j, q_j, and b_j collect like terms from Eq. 3.

In Eq. 3, the resonant size parameter was not expanded as function of r. The reason for this is that resonant size parameter is not well described as a linear function of r. This is illustrated in Fig. 2 for second order modes where $m_2 > m_1$ (Fig. 2a) and $m_1 > m_2$ (Fig. 2d). In those two examples, it can be seen that the resonant size parameter is not linear with r. In contrast, when r is fixed and either m_1 is varied (Fig. 2b and e) or m_2 is varied (Fig. 2c and f) the plotted resonant size parameters are approximately linear across fairly large ranges of both m_1 and m_2. Therefore, r will not be a parameter of best-fit in the least squares problem considered in this section. Instead, in the algorithm that will be subsequently developed, S will be tabulated as a function of r_0 and the value of r_0 that yields a minimum S will be taken as the r of best-fit.

Next, a parameterization for the refractive index is introduced. Here we choose to express the wavenumber-dependent refractive index of both the core ($s = 1$) or shell ($s = 2$) using the form of the Cauchy equation with $K_s + 1$ terms[45]

$$m_{sj} = \sum_{k=0}^{K_s} \alpha_{sk} \nu_j^{2k}, \tag{5}$$

where α_{sk} are the fitting parameters for the refractive index functions. With the definition of the refractive index from Eq. 5, the parameters of best-fit will be the set of a_2, α_{10}, α_{11}, ..., α_{1K_1}, α_{20}, α_{21}, ..., α_{2K_2}, and r that yield the smallest value of S in Eq. 1.

In Appendix A, a set of equations are constructed by inserting Eqs. 4 and 5 into Eq. 2 and setting the partial derivative of S with respect to each parameter to zero. The derived set of linear simultaneous equations for the error minimization problem can be written as

$$\mathbf{A} \cdot \mathbf{v} = \mathbf{d}, \tag{6}$$

where

$$\mathbf{v} = (a_2, \alpha_{10}, \alpha_{11}, \ldots, \alpha_{1K_1}, \alpha_{20}, \alpha_{21}, \ldots, \alpha_{2K_2})^{\mathsf{T}},$$

$$\mathbf{d} = -\left(\sum_j b_j^2, \sum_j b_j p_j, \sum_j b_j p_j \nu_j^2, \ldots, \sum_j b_j p_j \nu_j^{2K_1}, \sum_j b_j q_j, \sum_j b_j q_j \nu_j^2, \ldots, \sum_j b_j q_j \nu_j^{2K_2}\right)^{\mathsf{T}},$$

$$\mathbf{A} = \begin{bmatrix} -2\pi\sum \nu_j b_j & \sum p_j b_j & \sum p_j b_j \nu_j^2 & \cdots & \sum p_j b_j \nu_j^{2K_1} & \sum q_j b_j & \sum q_j b_j \nu_j^2 & \cdots & \sum q_j b_j \nu_j^{2K_2} \\ -2\pi\sum \nu_j p_j & \sum p_j^2 & \sum p_j^2 \nu_j^2 & \cdots & \sum p_j^2 \nu_j^{2K_1} & \sum q_j p_j & \sum q_j p_j \nu_j^2 & \cdots & \sum q_j p_j \nu_j^{2K_2} \\ -2\pi\sum \nu_j^3 p_j & \sum p_j^2 \nu_j^2 & \sum p_j^2 \nu_j^4 & \cdots & \sum p_j^2 \nu_j^{2K_1+2} & \sum q_j p_j \nu_j^2 & \sum q_j p_j \nu_j^4 & \cdots & \sum q_j p_j \nu_j^{2K_2+2} \\ \vdots & \vdots & \vdots & \ddots & \vdots & \vdots & \vdots & \ddots & \vdots \\ -2\pi\sum \nu_j^{2K_1+1} p_j & \sum p_j^2 \nu_j^{2K_1} & \sum p_j^2 \nu_j^{2K_1+2} & \cdots & \sum p_j^2 \nu_j^{4K_1} & \sum q_j p_j \nu_j^{2K_1} & \sum q_j p_j \nu_j^{2K_1+2} & \cdots & \sum q_j p_j \nu_j^{2K_1+2K_2} \\ -2\pi\sum \nu_j q_j & \sum q_j p_j & \sum q_j p_j \nu_j^2 & \cdots & \sum q_j p_j \nu_j^{2K_1} & \sum q_j^2 & \sum q_j^2 \nu_j^2 & \cdots & \sum q_j^2 \nu_j^{2K_2} \\ -2\pi\sum \nu_j^3 q_j & \sum q_j p_j \nu_j^2 & \sum q_j p_j \nu_j^4 & \cdots & \sum q_j p_j \nu_j^{2K_1+2} & \sum q_j^2 \nu_j^2 & \sum q_j^2 \nu_j^4 & \cdots & \sum q_j^2 \nu_j^{2K_2+2} \\ \vdots & \vdots & \vdots & \ddots & \vdots & \vdots & \vdots & \ddots & \vdots \\ -2\pi\sum \nu_j^{2K_2+1} q_j & \sum q_j p_j \nu_j^{2K_2} & \sum q_j p_j \nu_j^{2K_2+2} & \cdots & \sum q_j p_j \nu_j^{2K_1+2K_2} & \sum q_j^2 \nu_j^{2K_2} & \sum q_j^2 \nu_j^{2K_2+2} & \cdots & \sum q_j^2 \nu_j^{4K_2} \end{bmatrix}.$$

Solving Eq. 6 for $\mathbf{v}$ yields the parameters of best-fit. The necessary background for calculating p_j, q_j, and b_j is covered in the subsequent section along with Appendix B. Then, in Appendix C, it is shown how b_j, p_j, and q_j can be determined through the application of the chain rule to the resonance condition.

3 The core-shell resonance condition and its solution

The resonance condition for TE and TM modes for a spherical core with a concentric spherical shell is known to be[27]

$$\frac{j_n(m_2 z_1)\left(1 + m_1 z_1 j_n'(m_1 z_1)/j_n(m_1 z_1)\right) - w\left(j_n(m_2 z_1) + m_2 z_1 j_n'(m_2 z_1)\right)}{y_n(m_2 z_1)\left(1 + m_1 z_1 j_n'(m_1 z_1)/j_n(m_1 z_1)\right) - w\left(y_n(m_2 z_1) + m_2 z_1 y_n'(m_2 z_1)\right)} = \frac{j_n(m_2 z_2)\left(1 + z_2 h_n^{(1)\prime}(z_2)/h_n^{(1)}(z_2)\right) - v\left(j_n(m_2 z_2) + m_2 z_2 j_n'(m_2 z_2)\right)}{y_n(m_2 z_2)\left(1 + z_2 h_n^{(1)\prime}(z_2)/h_n^{(1)}(z_2)\right) - v\left(y_n(m_2 z_2) + m_2 z_2 y_n'(m_2 z_2)\right)}, \quad (7)$$

where z_1 and z_2 are a pair of complex resonant size parameters, whose respective real parts, x_1 and x_2, are related to ratio, r, through $r = x_1/x_2$. For TE polarization, the terms v and w are $v = 1$ and $w = 1$ and for TM polarization, $v = 1/m_2^2$ and $w = m_1^2/m_2^2$. The functions j_n and y_n are the spherical Bessel functions of the first and second kind, respectively, and $h_n^{(1)} = j_n + iy_n$

is the spherical Hankel function of the first kind. The derivatives, denoted by primes, are with respect to the arguments of their associated functions.

Solutions to Eq. 7 can be calculated numerically using a root-solving algorithm. The iterative Newton-Raphson method is one of the most well-known root-finding techniques and is used here. Its specific implementation for our case requires the evaluation of the resonance equation as well as its partial derivative with respect to both z_1 and z_2. This operation is not done directly with Eq. 7, however, instead we first re-express Eq. 7 as

$$\frac{\psi_n(m_2 z_1)\left[\frac{m_1}{m_2}\Psi_n(m_1 z_1) - w\Psi_n(m_2 z_1)\right]}{\chi_n(m_2 z_1)\left[\frac{m_1}{m_2}\Psi_n(m_1 z_1) - wX_n(m_2 z_1)\right]} = \frac{\psi_n(m_2 z_2)\left[\frac{1}{m_2}\Xi_n(z_2) - v\Psi_n(m_2 z_2)\right]}{\chi_n(m_2 z_2)\left[\frac{1}{m_2}\Xi_n(z_2) - vX_n(m_2 z_2)\right]}, \tag{8}$$

where $\psi_n(\rho) = \rho j_n(\rho)$, $\chi_n(\rho) = -\rho y_n(\rho)$, and $\xi_n(\rho) = \rho h_n^{(1)}(\rho)$ are known as the Riccati-Bessel functions[46] and Ψ_n, X_n, and Ξ_n are their associated logarithmic derivatives

$$\Psi_n(\rho) = \frac{\psi_n'(\rho)}{\psi_n(\rho)} = -\frac{n}{\rho} + \frac{j_{n-1}(\rho)}{j_n(\rho)}, \tag{9}$$

$$X_n(\rho) = \frac{\chi_n'(\rho)}{\chi_n(\rho)} = -\frac{n}{\rho} + \frac{y_{n-1}(\rho)}{y_n(\rho)}, \tag{10}$$

$$\Xi_n(\rho) = \frac{\xi_n'(\rho)}{\xi_n(\rho)} = -\frac{n}{\rho} + \frac{h_{n-1}^{(1)}(\rho)}{h_n^{(1)}(\rho)}. \tag{11}$$

The three logarithmic derivatives are similar in order of magnitude and are usually close to unity for large arguments. Numerically, this has the advantage that it eliminates the risk of an underflow or overflow error when comparing terms that are of different orders of magnitude.[47] After some manipulation, the derivative of Eq. 8 reduces to a relatively simple expression when compared to what is obtained when Eq. 7 is differentiated. The latter requires expanding the derivatives of the spherical Bessel functions using the recurrence relations[46]

$$(2n+1)f_n'(\rho) = nf_{n-1}(\rho) - (n+1)f_{n+1}(\rho), \tag{12}$$

$$(2n+1)f_n''(\rho) = nf_{n-1}'(\rho) - (n+1)f_{n+1}'(\rho), \tag{13}$$

where f_n is either j_n, y_n, or $h_n^{(1)}$. The number of terms needed to express the resonance equation and its derivative by directly applying the recurrence relations given in Eqs. 12 and 13 is significantly larger than the approach of recasting the resonance condition in terms of the logarithmic derivatives. Indeed, we have found that the logarithmic derivative approach is faster by about a factor of two when compared to the spherical Bessel function approach. In Appendix B, we provide expressions for the partial derivative of Eq. 8 with respect to both z_1 and z_2.

For a given m_1, m_2, r, n, and polarization, the core-shell resonance condition has an infinite number of solutions that correspond to different mode orders, l. Identifying the correct l for any one of these solutions is not trivial. Consequently, when applying the Newton-Raphson method to solve the resonance condition, an initial guess that is fairly close to the actual resonance for the desired mode order is required. In homogeneous spheres, this initial guess comes from a well-known approximate explicit formula.[33] As was discussed in the introduction, the analogous formulas for core-shell particles are only valid under very restrictive conditions and are unsuitable for most applications. One commonly used approach to determine core-shell resonances for the m_1, m_2, r, n, l and polarization of interest with the Newton-Raphson method is the following:[27,41] First, calculate the resonant size parameter for a homogeneous sphere with a refractive index m_1. This is straightforward[24] and serves as a suitable first guess when applying the Newton-Raphson method to solve Eq. 8 for a very thin shell. Once the accurate resonant size parameter of this thin shell system has been calculated it can subsequently be used as a first guess when calculating the resonant size parameter of a slightly thicker shell with the Newton-Raphson method. This iterative process can be continued until the desired r is reached.

While the above method allows for the accurate calculation of resonant size parameters in core-shell particles, its major drawback is its slow speed. During testing, it was found that the calculation of MDRs was the most significant bottleneck in the performance of our fitting program. This motivated us to develop an alternative approach based around changing m_2 in small steps rather than changing r in small steps. The advantage of this approach is that MDRs are approximately linear with m_1 (Fig. 2b and e) and m_2 (Fig. 2c and f) but not with r (Fig. 2a and d) for typical value ranges. This can be exploited in the root solving algorithm by using a first-order Taylor series to yield initial guesses for unknown solutions. The step size of the linear extrapolation when working with refractive index can be fairly coarse ($\sim 10^{-2}$ refractive index units).

Fig. 3 compares the time taken to compute the MDR position of the TE_{60}^{1} mode as a function of r for a core-shell particle where $m_1 = 1.60$ and $m_2 = 1.40$ using the approach where iterations in r are used and where iterations in m_2 are used. The computation time increases with shell thickness for the ratio method whereas the refractive index method is almost entirely insensitive to the shell thickness. Beyond very thin shells, it can be seen the method of iterating m_2 is much faster than the method of iterating r.

4 Discussion

An algorithm based on the solution to the error minimization problem presented in Section 2 and the method for calculating resonances in Section 3 was implemented in a Fortran program called MRSFIT. Similar to our previously developed fitting algorithm for homogeneous spheres,[24] the Fortran source code for MRSFIT will be made freely available.[48] In this section, the accuracy and applicability of the developed methodology is assessed using simulated modes

sets for core-shell particles. Two cases were considered: (i) the core refractive index is greater than the shell refractive index and (ii) the shell refractive index is greater than the core refractive index. The physically plausible wavelength-dependent refractive indices that were chosen were polystyrene[49] and water.[50] At optical wavelengths, the refractive index of polystyrene is always greater than that of water (e.g. at $\lambda = 0.645$ μm their refractive indices are 1.5864 and 1.3317, respectively).

Simulated modes sets were generated for r between 0.60 and 0.99 in steps of 0.01 by fixing the outer radius of the core-shell particle at $a_2 = 5$ μm. At each r, resonances located between $\lambda = 0.63$ and 0.66 μm were retained for the final mode set. This was done for both (i) $l = 1$ and $l = 2$ and (ii) $l = 2$ and $l = 3$ modes. For each pair of modes orders, the process resulted in 40 sets of modes for both $m_1 > m_2$ and $m_2 > m_1$. Each set would typically have about 12 modes for the chosen wavelength range. Gaussian noise with a deviation, σ_g, was then added to these noise-free mode sets and the resulting noisy mode sets were fitted using MRSFIT with a one-dimensional search from $r = 0.50$ to 1.00 in steps of 0.0001. Both the core and shell refractive index were fitted with three term Cauchy expressions ($K_1 = 2$ and $K_2 = 2$). The fitting process was repeated at each r with 20 different noisy sets in order to assess the accuracy and uncertainty of fitting core-shell resonances.

Fig. 4 shows the ratio of best-fit, $r_{\text{best-fit}}$, as a function of the true ratio, r_{true}. The values of σ_g applied to the mode sets were (a and b) 10^{-6} μm, (c and d) 10^{-5} μm, or (e and f) 10^{-4} μm. A typical uncertainty in the position of experimentally measured resonances is $\pm 10^{-5}$ μm,[51] so the chosen values of σ_g should be indicative of this figure of merit and values well above and well below it. In Fig. 4, we see that when fitting peak positions with typical experimental uncertainties, the value of $r_{\text{best-fit}}$ is accurate until the shell becomes fairly thick ($r_{\text{true}} < 0.75$).

We also see that the best-fits for the $l = 1$ and $l = 2$ sets become inaccurate at larger r_{true} than the best-fits for the $l = 2$ and $l = 3$ sets. Both of these results were anticipated: Once the shell becomes too thick, the resonance positions cease to significantly shift with decreasing r and are no longer a sensitive probe of shell thickness. Fig. 2a and d show examples of this for $l = 2$ modes where a plateau occurs for $r < 0.80$ in the case of $m_2 > m_1$ and $r < 0.75$ for $m_1 > m_2$. This plateau will occur at smaller r for increasing l as the peak mode energy will be located further from the outer surface of the shell (see Ref. 27 for further examples). Consequently, higher mode orders can probe thicker shells. Of course, when measuring optical spectra, MDR linewidth determines which resonances can be observed so one is not simply free to measure higher mode orders when attempting to characterize thicker shells.

Fig. 5 shows the refractive index of both the core and shell at a fixed wavelength as plotted as a function of r_{true}. The chosen wavelength was $\lambda = 0.645$ μm (the midpoint of the wavelength range used to select MDRs to be fitted). The explanation for the accuracy of the best-fits in Fig. 5 is similar to that given above for Fig. 4. However, it is interesting to note that for thick shells the best-fit for the shell refractive index can still be accurate despite the fact that the corresponding best-fit for r in Fig. 4 is inaccurate (e.g. compare Fig. 5e and f to Fig. 4c and d for $r_{\text{true}} < 0.70$). The reason being that the best-fit is essentially that of a homogeneous sphere with the shell refractive index. Also of note, is that when $m_1 > m_2$, the accuracy of the best-fits are much worse for thin shells ($r_{\text{true}} > 0.95$) than when $m_2 > m_1$. For instance, compare Fig. 5e and g to Fig. 5f and h. In the thin shell limit, MDRs are much less sensitive to the core and shell refractive indices when $m_1 > m_2$ and this yields poor best-fits. Similar observations have been reported previously for very thin shells ($r > 0.99$).[36]

In Figs. 6 and 7 the wavelength-dependent refractive index is plotted for $r_{\text{true}} = 0.90$ and

0.80, respectively. Because the range of MDRs chosen when generating the simulated sets was between $\lambda = 0.63$ and 0.66 μm, the uncertainty in the refractive index calculated with the parameters of best-fit increases greatly further away from this spectral window. This becomes more severe with increasing Gaussian noise. However, within the neighborhood of the window containing MDRs, the retrieved refractive index is in good agreement with the true value when the Gaussian noise is $\sigma_g = 10^{-5}$ μm or less. The one exception is the best-fit for m_2 when $l = 1$ and 2, $r_{\text{true}} = 0.90$, and $m_1 > m_2$ when $\sigma_g = 10^{-6}$ μm (Fig. 6a). However, for a realistic noise level ($\sigma_g = 10^{-5}$ μm, Fig. 6e) the accuracy of the best-fit is comparable to the other m_2 best-fits for $m_1 > m_2$. Note that decreasing the number of refractive index parameters from three to two (results not shown here) did not have any significant effect on the retrieved best-fits. As a further point of comparison, we provide the wavelength-dependent refractive index of best-fit for a homogeneous sphere in Fig. 8. Not only do the results for the homogeneous sphere always produce accurate results, but the uncertainty outside of the window containing MDR peaks is always as good or better than the lowest uncertainty in the core-shell best-fits.

In Fig. 9, the sum of the squared difference, S, divided by the number of modes, J, for the best-fit is plotted as a function of r for the set of MDRs where $r_{\text{true}} = 0.90$ and 0.80. These types of one-dimensional calculations are used by MRSFIT to identify $r_{\text{best-fit}}$ and the parameters of best-fit that are associated with that minimum in S/J (as was discussed in Section 2). In the plots, the depth of the minima become shallower with increasing Gaussian noise and at $\sigma_g = 10^{-4}$ μm cannot be identified on the log plot (either due to being very shallow or disappearing completely). In the previous paragraph we discussed the inaccurate best-fit for the case where r_{true}, $m_1 > m_2$, and $l = 1$ and 2 when $\sigma_g = 10^{-6}$ μm. In Fig. 9a we see that, for all noise levels, there is no minimum within the plotted range of r. However, the minima are

actually all fairly close to the true value of r. For instance, for $\sigma_g = 10^{-6}$ μm, the minimum is located at $r = 0.8978$. The consequence of this seemingly small deviation from the true value is the previously mentioned inaccuracy in the best-fit for the shell refractive index (Fig. 6a). In contrast, the core refractive index is very close to its true value within the chosen MDR range (Fig. 6c). The main result from Fig. 9 concerns the required step size in r that should be used with MRSFIT. Steps in r of 0.0001 are fine enough to correctly identify the location of global minima in S/J for typical experimental uncertainties of $\pm 10^{-5}$ μm.

Next, we consider MDR sets that contain only a single mode order. Sets where $l = 1$, 2, or 3 were generated using the same procedure outlined above. However, the wavelength range over which MDRs were retained was set from $\lambda = 0.615$ to 0.675 μm in order to ensure that the number of modes in each set was usually around 12 (similar in number to that of the multiple mode order sets). Fig. 10 shows the best-fits from MRSFIT for these single mode order sets when $\sigma_g = 10^{-6}$ μm. Despite the small value of σ_g, the accuracy of the best-fits is very poor. This result is surprising as fitting MDR sets that contain only a single mode order is routine for homogeneous spheres and is known to yield accurate fits.[24] Reducing the noise further on the single mode order sets will eventually lead to accurate fits, so we can conclude that best-fits from MDR sets that contain only a single mode order are much more sensitive to uncertainty in measured peak positions than sets with multiple mode orders. Unfortunately, the required uncertainty ($\sigma_g < 10^{-6}$ μm) is well below that which is currently achievable through conventional spectroscopic methods. Therefore, for MDR sets with only a single mode order, accurate fits for core-shell particles are unlikely to be realizable unless the parameter space is restricted in some way (e.g. one or more of the parameters are known beforehand).

Finally, we examine how incorrect mode assignments affect the fitting of MDR sets. Fig. 11

shows the effect that systematically offsetting the mode number from a correct mode assignment has on the parameters of best-fit. In Fig. 11a and b, the incorrect assignment has relatively little impact on $r_{\text{best-fit}}$ except across the smaller values of r_{true} that are plotted. In contrast, Fig. 11c and d shows that the outer radius fit is biased for nearly all values of r_{true} (and that the inaccuracy becomes greater as the mode number offset increases). This bias extends to the fitted values of the core refractive index (Fig. 11e and f) and the shell refractive index (Fig. 11g and h). The result of greatest interest, though, is how S/J changes with the mode offset. Fig. 11i and j show S/J as a function of r_{true}. For $m_2 > m_1$ (Fig. 11j), S/J for the correct mode assignment is lower than almost all of the incorrect mode assignments. However, for the case where $m_1 > m_2$ (Fig. 11i), this is not the case as incorrect mode assignments often yield S/J lower than the correct mode assignment. The implication of this result is that one should not always assume that the mode assignment that gives the lowest S/J is the correct mode assignment. This may cause inaccuracies if the mode assignment is not known beforehand and several reasonable possibilities are being considered during the fitting process. For the cases studied here, this appears to be a more significant issue when $m_1 > m_2$.

5 Conclusion

We have thoroughly examined the problem of characterizing the size and composition of a core-shell particle using measured MDR positions. For our analysis we utilized a new fitting algorithm that was based on solving a least squares problem. Simultaneously, to rapidly calculate MDR positions, we developed a new scheme based around iterating shell refractive index rather than shell thickness. The Fortran implementation of our fitting algorithm, a program called MRSFIT, will be made freely available.[48] Fitting MDR sets with typical experimental

uncertainties showed that accurate fits for both the size and refractive index of the core and shell could be found with MRSFIT although there were exceptions; the most notable one being that MDR sets with only one mode order did not yield good best-fits. For the search parameters used here, MRSFIT could complete the fitting process for a single MDR set in well under an hour on an Intel Xeon CPU E5-1620 v4 at 3.50 GHz. If the same MDR set was fitted using a grid search across the same parameter space it would require searching an eight-dimensional grid and would not be feasible without greatly restricting the search space (see Ref. 38 for an example of the severe restrictions that were necessary to perform a grid search when fitting core-shell MDRs). This is different than the situation with homogeneous spheres where grid searches are in fact feasible (although they are still much slower than the least squares method). Therefore, we anticipate that the program implemented here and the insights presented in our discussion will be invaluable for high-precision spectroscopic studies of core-shell particles.

A Appendix

Inserting Eq. 4 and 5 into Eq. 2 and setting the partial derivative of S with respect to each parameter to zero yields the following set of equations:

$$\begin{aligned}
\frac{\partial S}{\partial a_2} &= 2\sum_j \left(\nu_j - \frac{p_j m_{1j} + q_j m_{2j} + b_j}{2\pi a_2}\right)\left(\frac{p_j m_{1j} + q_j m_{2j} + b_j}{2\pi a_2^2}\right) = 0, \\
\frac{\partial S}{\partial \alpha_{10}} &= 2\sum_j \left(\nu_j - \frac{p_j m_{1j} + q_j m_{2j} + b_j}{2\pi a_2}\right)\left(-\frac{p_j}{2\pi a_2}\right) = 0, \\
\frac{\partial S}{\partial \alpha_{11}} &= 2\sum_j \left(\nu_j - \frac{p_j m_{1j} + q_j m_{2j} + b_j}{2\pi a_2}\right)\left(-\frac{p_j \nu_j^2}{2\pi a_2}\right) = 0, \\
&\vdots \\
\frac{\partial S}{\partial \alpha_{1K_1}} &= 2\sum_j \left(\nu_j - \frac{p_j m_{1j} + q_j m_{2j} + b_j}{2\pi a_2}\right)\left(-\frac{p_j \nu_j^{2K_1}}{2\pi a_2}\right) = 0, \\
\frac{\partial S}{\partial \alpha_{20}} &= 2\sum_j \left(\nu_j - \frac{p_j m_{1j} + q_j m_{2j} + b_j}{2\pi a_2}\right)\left(-\frac{q_j}{2\pi a_2}\right) = 0, \\
\frac{\partial S}{\partial \alpha_{21}} &= 2\sum_j \left(\nu_j - \frac{p_j m_{1j} + q_j m_{2j} + b_j}{2\pi a_2}\right)\left(-\frac{q_j \nu_j^2}{2\pi a_2}\right) = 0, \\
&\vdots \\
\frac{\partial S}{\partial \alpha_{2K_2}} &= 2\sum_j \left(\nu_j - \frac{p_j m_{1j} + q_j m_{2j} + b_j}{2\pi a_2}\right)\left(-\frac{q_j \nu_j^{2K_2}}{2\pi a_2}\right) = 0,
\end{aligned} \tag{A1}$$

The equations generated from $\partial S/\partial \alpha_{nk}$ are linear and the equation generated from $\partial S/\partial a_2$ can also be simplified to a linear equation by using the method from Ref. 24. This yields

$$\frac{\partial S}{\partial a_2} = 2\sum_j \left(\nu_j - \frac{p_j m_{1j} + q_j m_{2j} + b_j}{2\pi a_2}\right)\left(\frac{b_j}{2\pi a_2^2}\right) = 0. \tag{A2}$$

With this result, system A1 can now be written as the following set of linear equations:

$$\begin{aligned}
&\sum_j \left(2\pi a_2\nu_j - (p_j m_{1j} + q_j m_{2j} + b_j)\right) b_j = 0,\\
&\sum_j \left(2\pi a_2\nu_j - (p_j m_{1j} + q_j m_{2j} + b_j)\right) p_j = 0,\\
&\sum_j \left(2\pi a_2\nu_j - (p_j m_{1j} + q_j m_{2j} + b_j)\right) p_j\nu_j^2 = 0,\\
&\qquad\qquad\vdots\\
&\sum_j \left(2\pi a_2\nu_j - (p_j m_{1j} + q_j m_{2j} + b_j)\right) p_j\nu_j^{2K_1} = 0,\\
&\sum_j \left(2\pi a_2\nu_j - (p_j m_{1j} + q_j m_{2j} + b_j)\right) q_j = 0,\\
&\sum_j \left(2\pi a_2\nu_j - (p_j m_{1j} + q_j m_{2j} + b_j)\right) q_j\nu_j^2 = 0,\\
&\qquad\qquad\vdots\\
&\sum_j \left(2\pi a_2\nu_j - (p_j m_{1j} + q_j m_{2j} + b_j)\right) q_j\nu_j^{2K_2} = 0.
\end{aligned} \tag{A3}$$

After some further manipulation, system A3 can be more compactly written as Eq. 6.

B Appendix

Here we provide expressions for the partial derivatives $\partial f/\partial z_1$ and $\partial f/\partial z_2$ that we use in our Newton-Raphson algorithm. First, however, we note that Eq. 8 is more stable if we multiply both sides by the denominators to yield

$$\begin{aligned}
&\psi_n(m_2 z_1)\left[\widetilde{\Psi}_n(m_1 z_1) - w\Psi_n(m_2 z_1)\right]\chi_n(m_2 z_2)\left[\widetilde{\Xi}_n(z_2) - vX_n(m_2 z_2)\right]\\
&\quad - \psi_n(m_2 z_2)\left[\widetilde{\Xi}_n(z_2) - v\Psi_n(m_2 z_2)\right]\chi_n(m_2 z_1)\left[\widetilde{\Psi}_n(m_1 z_1) - wX_n(m_2 z_1)\right] = 0,
\end{aligned} \tag{B1}$$

where we have now introduced $\widetilde{\Psi}_n = m_1\Psi_n/m_2$ and $\widetilde{\Xi}_n = \Xi_n/m_2$.

The Riccati-Bessel functions, denoted as ω, are solutions to the Riccati differential equation:[52]

$$\rho^2\omega_n''(\rho) + [\rho^2 - n(n+1)]\omega_n(\rho) = 0. \tag{B2}$$

We define $\Omega_n(\rho) = \omega_n'(\rho)/\omega_n(\rho)$, so that the derivative of $\Omega_n(\rho)$ is

$$\Omega_n'(\rho) = \frac{\omega_n''(\rho)}{\omega_n(\rho)} - \frac{\omega_n'(\rho)^2}{\omega_n(\rho)^2}. \tag{B3}$$

Using Eq. B2 and the definition of $\Omega_n(\rho)$ gives

$$\Omega_n'(\rho) = \frac{n(n+1)}{\rho^2} - \Omega_n^2(\rho) - 1. \tag{B4}$$

One last result is helpful. Consider the derivative of one of the four terms in Eq. B1, e.g. the term

$$\psi_n(m_2z_1)\left[\widetilde{\Psi}_n(m_1z_1) - w\Psi_n(m_2z_1)\right], \tag{B5}$$

whose derivative with respect to z_1 is

$$\psi_n(m_2z_1)\left[[m_1\widetilde{\Psi}_n'(m_1z_1) - wm_2\Psi_n'(m_2z_1)] + m_2\frac{\psi_n'(m_2z_1)}{\psi_n(m_2z_1)}[\widetilde{\Psi}_n(m_1z_1) - w\Psi_n(m_2z_1)]\right]. \tag{B6}$$

If we substitute $\Psi_n(m_2z_1) = \psi_n'(m_2z_1)/\psi_n(m_2z_1)$ and Eq. B4 into Eq. B6 we get

$$m_2\psi_n(m_2z_1)\left[\widetilde{\Psi}_n(m_1z_1)(\Psi_n(m_2z_1) - \widetilde{\Psi}_n(m_1z_1)) + (1-w)\frac{n(n+1)}{(m_2z_1)^2} + w - \frac{m_1^2}{m_2^2}\right]. \tag{B7}$$

Similar substitutions can be made to simplify the derivatives of the other terms in Eq. B1.

It is worthwhile to note here that $(1-w)n(n+1)/(m_2z_1)^2 = 0$ for TE polarization while $w - m_1^2/m_2^2 = 0$ for TM polarization. Because the four terms in Eq. B1 are similar in form, we

can subsequently write down the partial derivatives of f with respect to z_1 and z_2 as

$$\frac{\partial f}{\partial z_1} = m_2\psi_n(m_2z_1)\left[\widetilde{\Psi}_n(m_1z_1)(\Psi_n(m_2z_1)-\widetilde{\Psi}_n(m_1z_1))+A_w\right] \times \chi_n(m_2z_2)\left[\widetilde{\Xi}_n(z_2)-vX_n(m_2z_2)\right]-\psi_n(m_2z_2)\left[\widetilde{\Xi}_n(z_2)-v\Psi_n(m_2z_2)\right] \times m_2\chi_n(m_2z_1)\left[\widetilde{\Psi}_n(m_1z_1)(X_n(m_2z_1)-\widetilde{\Psi}_n(m_1z_1))+A_w\right], \quad \text{(B8)}$$

$$\frac{\partial f}{\partial z_2} = m_2\chi_n(m_2z_2)\left[\widetilde{\Xi}_n(z_2)(X_n(m_2z_2)-\widetilde{\Xi}_n(z_2))+B_v\right] \times \psi_n(m_2z_1)\left[\widetilde{\Psi}_n(m_1z_1)-w\Psi_n(m_2z_1)\right]-\chi_n(m_2z_1)\left[\widetilde{\Psi}_n(m_1z_1)-wX_n(m_2z_1)\right] \times m_2\psi_n(m_2z_2)\left[\widetilde{\Xi}_n(z_2)(\Psi_n(m_2z_2)-\widetilde{\Xi}_n(z_2))+B_v\right], \quad \text{(B9)}$$

where $A_w = (1-w)n(n+1)/(m_2z_1)^2+(w-m_1^2/m_2^2)$ and $B_v = (1-v)n(n+1)/(m_2z_2)^2+(v-1/m_2^2)$.

C Appendix

In this Appendix we give expressions for p_j, q_j, and b_j that are used in the implementation of our fitting algorithm. The partial derivative of the resonant size parameter as a function of the core or shell refractive index can be found by considering the left-hand side of Eq. B1, denoted for brevity as f here, and its differential

$$df = \frac{\partial f}{\partial m_1}dm_1 + \frac{\partial f}{\partial m_2}dm_2 + \left(r\frac{\partial f}{\partial z_1}+\frac{\partial f}{\partial z_2}\right)dz_2, \quad \text{(C1)}$$

where we have made use of $dz_1 = rdz_2$. When perturbing either m_1 or m_2 for a fixed r, it must be true that the change in z_1 and z_2 satisfy $df = 0$. This gives the following expression

$$\frac{dz_2}{dm_s} = -\frac{\partial f}{\partial m_s}\left(r\frac{\partial f}{\partial z_1}+\frac{\partial f}{\partial z_2}\right)^{-1}, \quad \text{(C2)}$$

where s is either 1 or 2. This chain rule gives the partial derivative of the resonant size parameter z_2 as a function of m_1 and m_2, the results of which can be used to determine p_j and

q_j. The partial derivatives $\partial f/\partial z_1$, $\partial f/\partial z_2$ were already given in Appendix B (Eq. B8 and B9). Therefore, we only require expressions for $\partial f/\partial m_s$ here. The procedure is similar to that outlined in Appendix B, with the added complexity that v and w can depend on m_1 and m_2 for the TM polarization (as $v = 1/m_2^2$ and $w = m_1^2/m_2^2$). The partial derivative with respect to m_1 is

$$\begin{aligned}\left(\frac{\partial f}{\partial m_1}\right)_{\mathrm{TM}} &= \frac{\psi_n(m_2 z_1)}{m_1}[\widetilde{\Psi}_n(m_1 z_1)(1 - m_2 z_1 \widetilde{\Psi}_n(m_1 z_1)) + \frac{n(n+1)}{m_2 z_1} - \frac{m_1^2 z_1}{m_2} - 2w\Psi_n(m_2 z_1)] \\ &\times \chi_n(m_2 z_2)[\widetilde{\Xi}_n(z_2) - vX_n(m_2 z_2)] - \psi_n(m_2 z_2)[\widetilde{\Xi}_n(z_2) - v\Psi_n(m_2 z_2)] \\ &\times \frac{\chi_n(m_2 z_1)}{m_1}[\widetilde{\Psi}_n(m_1 z_1)(1 - m_2 z_1 \widetilde{\Psi}_n(m_1 z_1)) + \frac{n(n+1)}{m_2 z_1} - \frac{m_1^2 z_1}{m_2} - 2wX_n(m_2 z_1)].\end{aligned} \tag{C3}$$

The analogous expression for the TE polarization can be found by recognizing that the terms $2w\Psi_n(m_2 z_1)$ and $2wX_n(m_2 z_1)$ in Eq. C3 would be zero in that case. The equation for the partial derivative with respect to m_2 is more lengthy. It is

$$\begin{aligned}\left(\frac{\partial f}{\partial m_2}\right)_{\mathrm{TM}} &= \frac{\psi_n(m_2 z_1)}{m_2}[\widetilde{\Psi}_n(m_1 z_1)(m_2 z_1 \Psi_n(m_2 z_1) - 1) + w(2\Psi_n(m_2 z_1) + (m_2 z_1) - \frac{n(n+1)}{m_2 z_1})] \\ &\times \chi_n(m_2 z_2)[\Xi_n(z_2) - vX_n(m_2 z_2)] + \psi_n(m_2 z_1)[\Psi_n(m_1 z_1) - q\Psi_n(m_2 z_1)] \\ &\times \frac{\chi_n(m_2 z_2)}{m_2}[\widetilde{\Xi}_n(z_2)(m_2 z_2 X_n(m_2 z_2) - 1) + v(2X_n(m_2 z_2) + (m_2 z_2) - \frac{n(n+1)}{m_2 z_2})] \\ &- \frac{\psi_n(m_2 z_2)}{m_2}[\widetilde{\Xi}_n(z_2)(m_2 z_2 \Psi_n(m_2 z_2) - 1) + v(2\Psi_n(m_2 z_2) + (m_2 z_2) - \frac{n(n+1)}{m_2 z_2})] \\ &\times \chi_n(m_2 z_1)[\widetilde{\Psi}_n(m_1 z_1) - wX_n(m_2 z_1)] - \psi_n(m_2 z_2)[\widetilde{\Xi}_n(z_2) - v\Psi_n(m_2 z_2] \\ &\times \frac{\chi_n(m_2 z_1)}{m_2}[\widetilde{\Psi}_n(m_1 z_1)(m_2 z_1 X_n(m_2 z_1) - 1) + w(2X_n(m_2 z_1) + (m_2 z_1) - \frac{n(n+1)}{m_2 z_1})].\end{aligned} \tag{C4}$$

Again, an analogous expression for the TE polarization can be found by recognizing that the terms $2\Psi_n(m_2 z_1)$, $2\Psi_n(m_2 z_2)$, $2X_n(m_2 z_1)$, and $2X_n(m_2 z_2)$ are zero in that case.

In Section 2, we considered a set of J resonance positions. If z_2 in the above analysis is the size parameter for the jth resonance, z_{2j}, then its real part will be x_{2j}. Additionally, m_1 and m_2 at this resonance will be m_{1j} and m_{2j}, respectively. Then, the real part of the partial derivatives in Eqs. C3 and C4 (and their analogous expressions for TE polarization) will be equal to p_j and q_j, respectively. Once p_j and q_j are known at x_{2j}, the linear intercept b_j can be quickly calculated using

$$b_j = x_{2j} - p_j m_{1j} - q_j m_{2j}. \tag{C5}$$

Acknowledgements

T.C.P. acknowledges support from the Natural Sciences and Engineering Research Council of Canada (NSERC).

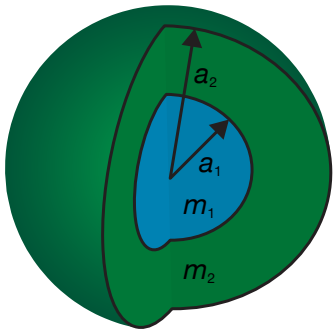

Figure 1: Illustration of the core-shell geometry discussed in this work (a spherical core with a concentric spherical shell). The radius of the core is a_1 and the radius of the shell is a_2. The refractive index of the core is m_1 and the radius of the shell is m_2.

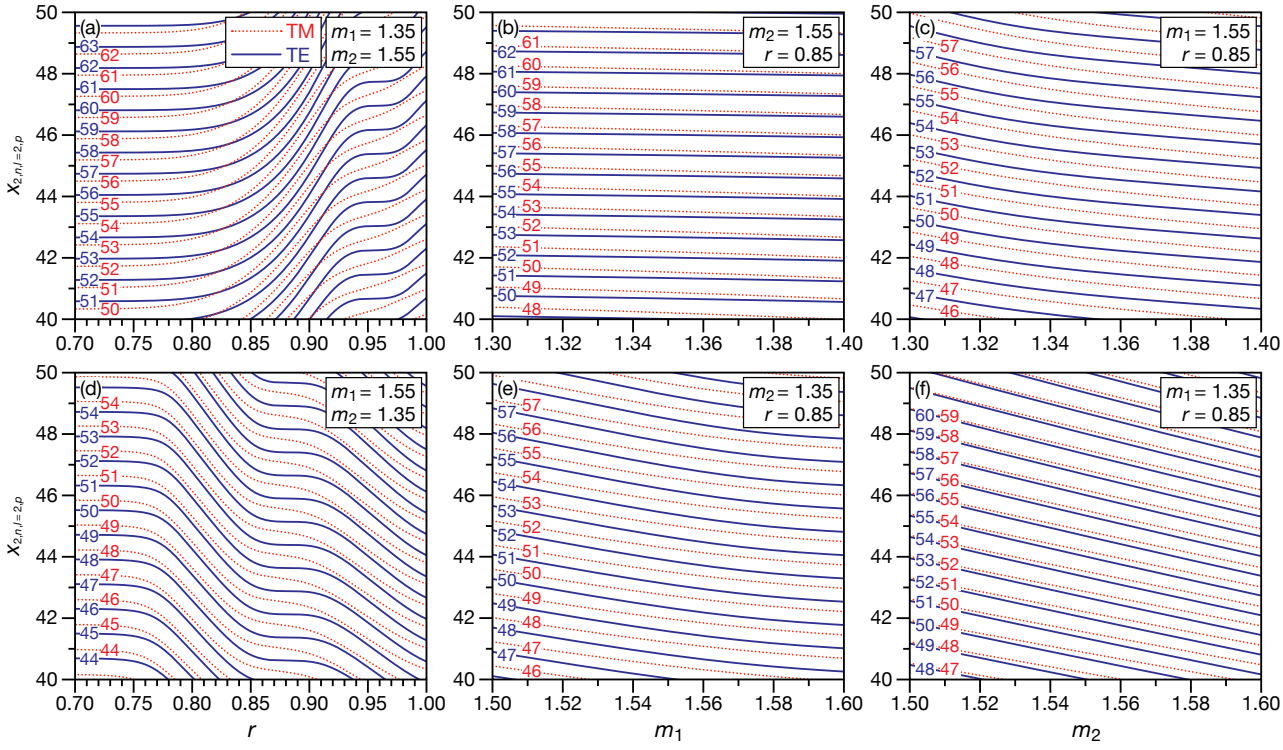

Figure 2: Second order MDR positions between size parameters 40 and 50 as a function of the (a and d) ratio between the radius of the core and the radius of the shell, r, (b and e) core refractive index, m_1, and (c and f) shell refractive index, m_2.

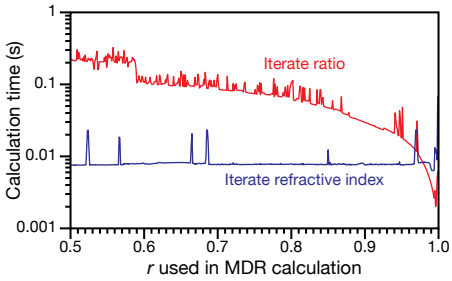

Figure 3: Time required to calculate the MDR position of a TE_{60}^{1} mode as a function of the ratio between the radius of the core and the radius of the shell, r. In this calculation, the core refractive index, m_1, was 1.60 and the shell refractive index, m_2, was 1.40. See Section 3 for a description of the algorithm that underlies the two methods that are being compared here. Calculations were performed using an Intel Xeon CPU E5-1620 v4 at 3.50 GHz.

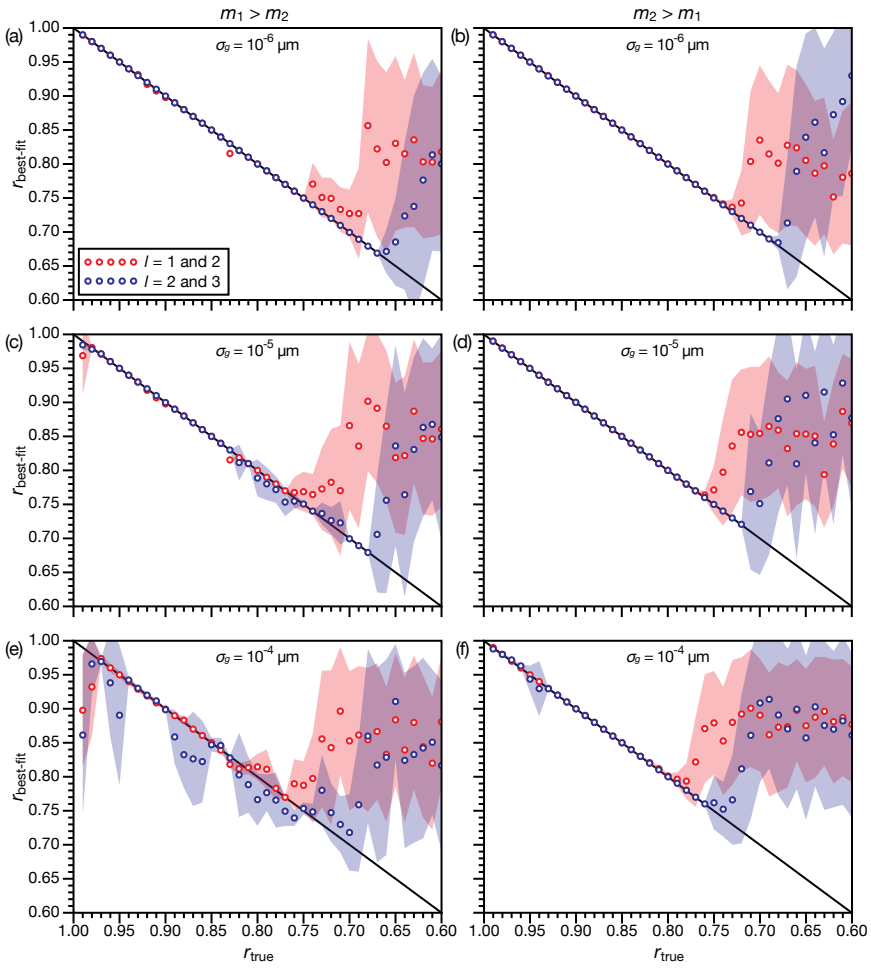

Figure 4: The ratio of best-fit, $r_{\text{best-fit}}$, as a function of the true ratio, r_{true}, determined by fitting simulated sets of MDR positions using the MRSFIT algorithm. See Section 4 for a detailed description of how the simulated MDR sets were generated. For panels on the left-hand side, the core was polystyrene and the shell was water. For panels on the right-hand side, the core was water and the shell was polystyrene. Best-fits for MDR sets containing either (i) first and second order or (ii) second and third order modes are shown here. Gaussian noise, σ_g, of (a and b) 10^{-6} μm, (c and d) 10^{-5} μm, or (e and f) 10^{-4} μm was applied to the MDR sets. The standard deviation in $r_{\text{best-fit}}$ is shown as a shaded region.

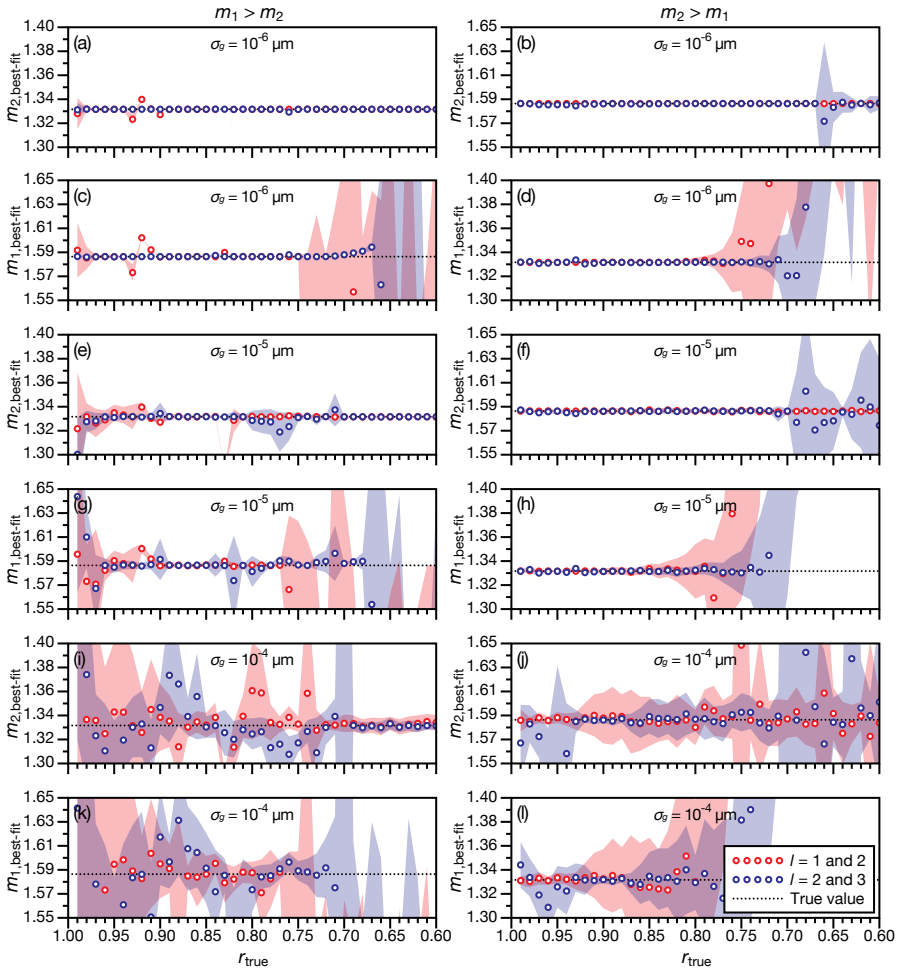

Figure 5: The refractive index of best-fit at $\lambda = 0.645$ μm for both the core and shell as a function of the true ratio, r_{true}, determined by fitting simulated sets of MDR positions using the MRSFIT algorithm. See Section 4 for a detailed description of how the simulated MDR sets were generated. For panels on the left-hand side, the core was polystyrene and the shell was water. For panels on the right-hand side, the core was water and the shell was polystyrene. Best-fits for MDR sets containing either (i) first and second order or (ii) second and third order modes are shown here. Gaussian noise, σ_g, of (a-d) 10^{-6} μm, (e-h) 10^{-5} μm, or (i-l) 10^{-4} μm was applied to the MDR sets. The standard deviation in $r_{\text{best-fit}}$ is shown as a shaded region.

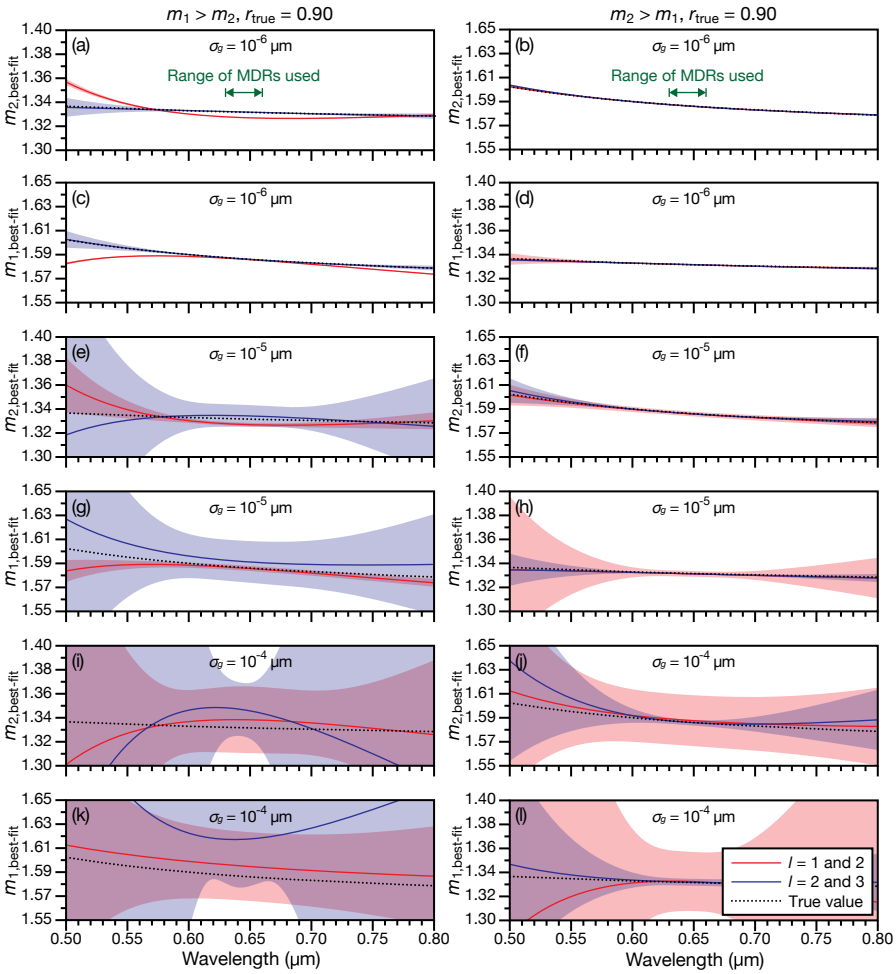

Figure 6: The wavelength-dependent refractive index of best-fit for both the core and shell determined by fitting simulated sets of MDR positions using the MRSFIT algorithm. The true ratio, r_{true}, is 0.90. See Section 4 for a detailed description of how the simulated MDR sets were generated. For panels on the left-hand side, the core was polystyrene and the shell was water. For panels on the right-hand side, the core was water and the shell was polystyrene. Best-fits for MDR sets containing either (i) first and second order or (ii) second and third order modes are shown here. Gaussian noise, σ_g, of (a-d) 10^{-6} μm, (e-h) 10^{-5} μm, or (i-l) 10^{-4} μm was applied to the MDR sets. The standard deviation in $r_{\text{best-fit}}$ is shown as a shaded region.

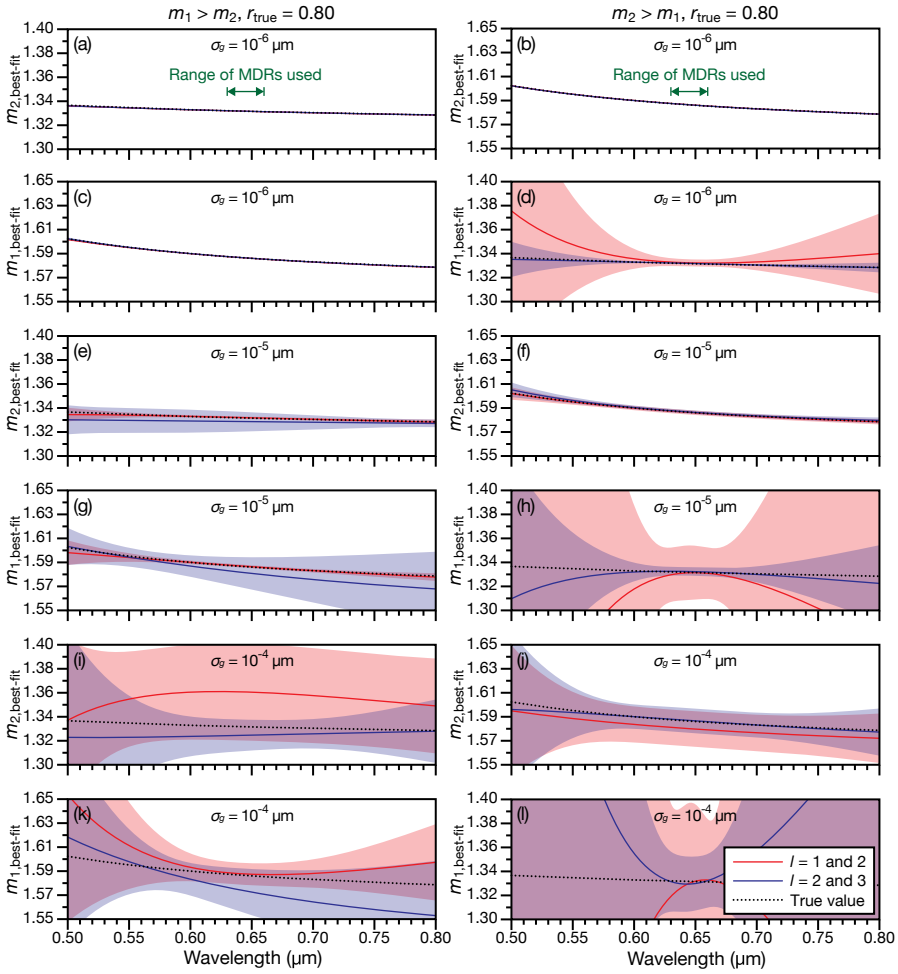

Figure 7: The wavelength-dependent refractive index of best-fit for both the core and shell determined by fitting simulated sets of MDR positions using the MRSFIT algorithm. The true ratio, r_{true}, is 0.80. See Section 4 for a detailed description of how the simulated MDR sets were generated. For panels on the left-hand side, the core was polystyrene and the shell was water. For panels on the right-hand side, the core was water and the shell was polystyrene. Best-fits for MDR sets containing either (i) first and second order or (ii) second and third order modes are shown here. Gaussian noise, σ_g, of (a-d) 10^{-6} μm, (e-h) 10^{-5} μm, or (i-l) 10^{-4} μm was applied to the MDR sets. The standard deviation in $r_{\text{best-fit}}$ is shown as a shaded region.

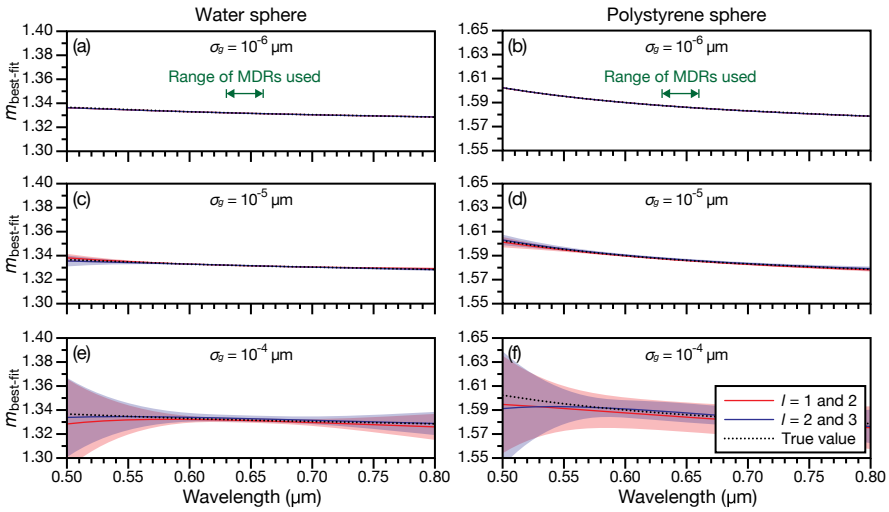

Figure 8: The wavelength-dependent refractive index of best-fit for a homogeneous sphere determined by fitting simulated sets of MDR positions using the MRFIT algorithm. See Section 4 for a detailed description of how the simulated MDR sets were generated. For panels on the left-hand side, the sphere was water. For panels on the right-hand side, the sphere was polystyrene. Best-fits for MDR sets containing either (i) first and second order or (ii) second and third order modes are shown here. Gaussian noise, σ_g, of (a and b) 10^{-6} μm, (c and d) 10^{-5} μm, or (e and f) 10^{-4} μm was applied to the MDR sets. The standard deviation in $r_{\text{best-fit}}$ is shown as a shaded region.

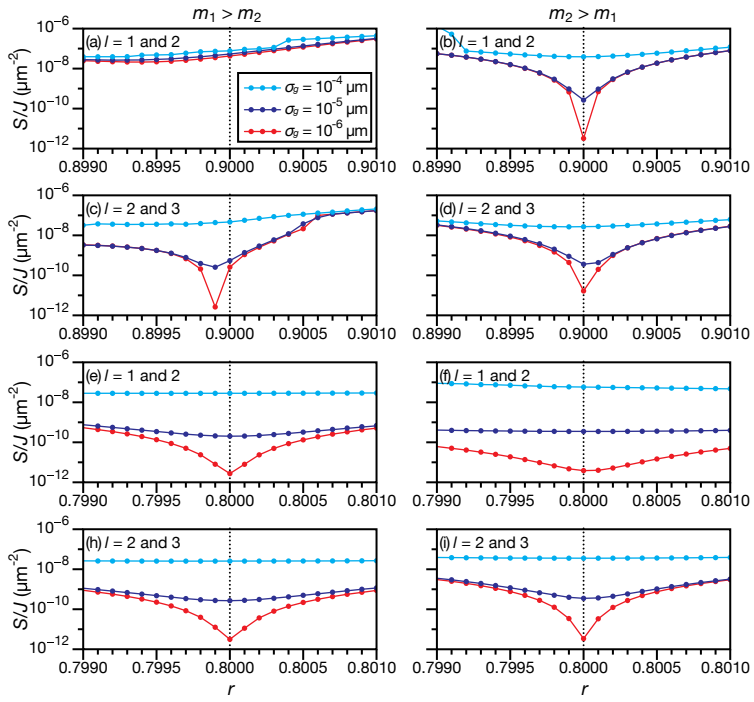

Figure 9: The sum of squared difference, S, for the best-fit divided by the number of resonance positions, J, being fitted as a function of the ratio, r. The Gaussian noise, σ_g, that was applied to the MDR sets either (a, b, e, and f) first and second order or (c, d, h, and j) second and third order modes was either 10^{-4} μm (light blue), 10^{-5} μm (dark blue), or 10^{-6} μm (red). or panels on the left-hand side, the core was polystyrene and the shell was water. For panels on the right-hand side, the core was water and the shell was polystyrene. Values of S/J shown are the average from fitting 20 MDR sets with the same value of σ_g. The vertical dotted line indicates the location of the true value of r.

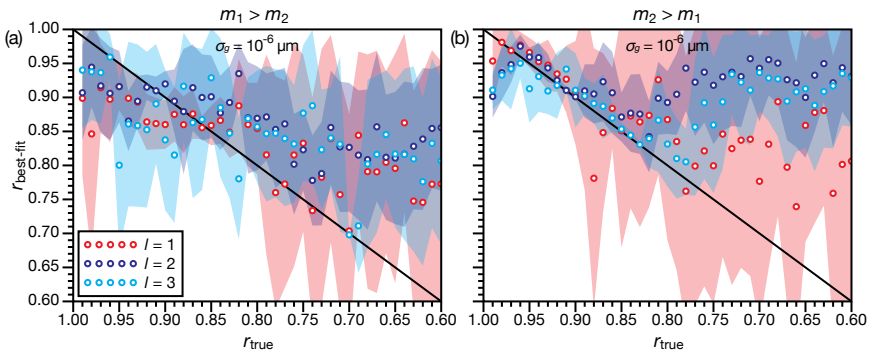

Figure 10: The ratio of best-fit, $r_{\text{best-fit}}$, as a function of the true ratio, r_{true}, determined by fitting simulated sets of MDR positions using the MRSFIT algorithm. See Section 4 for a detailed description of how the simulated MDR sets were generated. For panels on the left-hand side, the core was polystyrene and the shell was composed of water. For panels on the right-hand side, the core was water and the shell was composed of polystyrene. Best-fits for MDR sets containing either (i) first, (ii) second or (iii) third order modes are shown here. The Gaussian noise, σ_g, that was applied to the MDR sets was 10^{-6} μm. The standard deviation in $r_{\text{best-fit}}$ is shown as a shaded region.

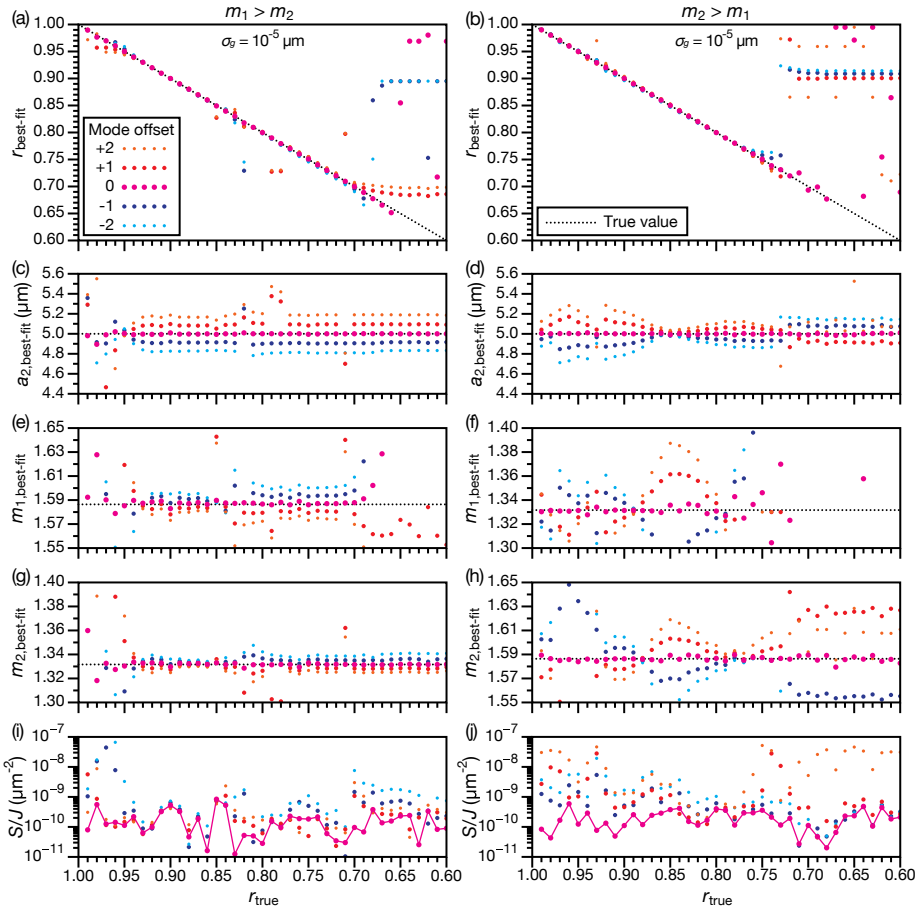

Figure 11: The effect of mode assignment on the best-fit. Parameters of best-fit (a-h) and S/J (i and j) as a function of of the true ratio, r_{true}, determined by fitting simulated sets of MDR positions using the MRSFIT algorithm. For panels on the left-hand side, the core was polystyrene and the shell was composed of water. For panels on the right-hand side, the core was water and the shell was composed of polystyrene. In each panel, five identical sets of MDR positions were fitted. However, the mode assignment of each set was systematically offset by adding either -2, -1, 0, 1, or 2 to the mode number, n, of the correct assignment (so an offset of 0 is the correct assignment). The Gaussian noise, σ_g, that was applied to all of the MDR sets was 10^{-5} μm. The refractive index of best-fit shown in (c-f) is calculated at $\lambda = 0.645$ μm. The MDR sets considered here contained only $l = 2$ and $l = 3$ modes.

References

1. Richtmyer, R. D. Dielectric resonators. *J. Appl. Phys.* **10**, 391–398 (1939).

2. Oraevsky, A. N. Whispering-gallery waves. *Quantum Electron.* **32**, 377–400 (2002).

3. Foreman, M. R., Swaim, J. D. & Vollmer, F. Whispering gallery mode sensors. *Adv. Opt. Photonics* **7**, 168–73 (2015).

4. Johnson, B. R. Theory of morphology-dependent resonances: shape resonances and width formulas. *J. Opt. Soc. Am. A:* **10**, 343–352 (1993).

5. Zheng, X. H. & Carroll, D. Exact resonant condition for dielectric spheres. *J. Opt. A: Pure Appl. Opt.* **1**, 168–172 (1999).

6. Ward, A. D., Zhang, M. & Hunt, O. Broadband Mie scattering from optically levitated aerosol droplets using a white LED. *Opt. Express* **16**, 16390–16403 (2008).

7. Moore, L. J., Summers, M. D. & Ritchie, G. A. D. Optical trapping and spectroscopic characterisation of ionic liquid solutions. *Phys. Chem. Chem. Phys.* **15**, 13489–13498 (2013).

8. Jones, S. H., King, M. D. & Ward, A. D. Determining the unique refractive index properties of solid polystyrene aerosol using broadband Mie scattering from optically trapped beads. *Phys. Chem. Chem. Phys.* **15**, 20735–20741 (2013).

9. Jones, S. H., King, M. D. & Ward, A. D. Atmospherically relevant core–shell aerosol studied using optical trapping and Mie scattering . *Chem. Commun.* **51**, 4914–4917 (2015).

10. David, G., Esat, K., Hartweg, S., Cremer, J., Chasovskikh, E. & Signorell, R. Stability of

aerosol droplets in Bessel beam optical traps under constant and pulsed external forces. *J. Chem. Phys.* **142**, 154506 (2015).

11. David, G., Esat, K., Ritsch, I. & Signorell, R. Ultraviolet broadband light scattering for optically-trapped submicron-sized aerosol particles. *Phys. Chem. Chem. Phys.* **18**, 5477–5485 (2016).

12. Lew, L. J. N., Ting, M. V. & Preston, T. C. Determining the size and refractive index of homogeneous spherical aerosol particles using Mie resonance spectroscopy. *Appl. Opt.* **57**, 4601–4609 (2018).

13. Benner, R. E., Barber, P. W., Owen, J. F. & Chang, R. K. Observation of structure resonances in the fluorescence spectra from microspheres. *Phys. Rev. Lett.* **44**, 475–478 (1980).

14. Tzeng, H. M., Wall, K. F., Long, M. B. & Chang, R. K. Evaporation and condensation rates of liquid droplets deduced from structure resonances in the fluorescence spectra. *Opt. Lett.* **9**, 273–275 (1984).

15. Campillo, A. J., Eversole, J. D. & Lin, H.-B. Cavity quantum electrodynamic enhancement of stimulated emission in microdroplets. *Phys. Rev. Lett.* **67**, 437–440 (1991).

16. Eversole, J. D., Lin, H.-B., Huston, A. L., Campillo, A. J., Leung, P. T., Liu, S. Y. & Young, K. High-precision identification of morphology-dependent resonances in optical processes in microdroplets. *J. Opt. Soc. Am. B: Opt. Phys.* **10**, 1955–1968 (1993).

17. Bischler, R., Olszyna, M., Himmelhaus, M. & Dähne, L. Development of a fully auto-

mated in-vitro diagnostics system based on low-Q whispering gallery modes in fluorescent microparticles. *Eur. Phys. J.* **223**, 2041–2055 (2014).

18. Vaughn, B. S., Tracey, P. J. & Trevitt, A. J. Drop-on-demand microdroplet generation: a very stable platform for single-droplet experimentation. *RSC Adv.* **6**, 60215–60222 (2016).

19. Snow, J. B., Qian, S. X. & Chang, R. K. Stimulated Raman scattering from individual water and ethanol droplets at morphology-dependent resonances. *Opt. Lett.* **10**, 37–39 (1985).

20. Schweiger, G. Raman scattering on single aerosol particles and on flowing aerosols: a review. *J. Aerosol Sci.* **21**, 483–509 (1990).

21. Symes, R., Sayer, R. M. & Reid, J. P. Cavity enhanced droplet spectroscopy: Principles, perspectives and prospects. *Phys. Chem. Chem. Phys.* **6**, 474–487 (2004).

22. Mitchem, L., Buajarern, J., Hopkins, R. J., Ward, A. D., Gilham, R. J., Johnston, R. L. & Reid, J. P. Spectroscopy of growing and evaporating water droplets: exploring the variation in equilibrium droplet size with relative humidity. *J. Phys. Chem. A* **110**, 8116–8125 (2006).

23. Preston, T. C. & Reid, J. P. Accurate and efficient determination of the radius, refractive index, and dispersion of weakly absorbing spherical particle using whispering gallery modes. *J. Opt. Soc. Am. B: Opt. Phys.* **30**, 2113–2122 (2013).

24. Preston, T. C. & Reid, J. P. Determining the size and refractive index of microspheres using the mode assignments from Mie resonances. *J. Opt. Soc. Am. A* **32**, 2210–2217 (2015).

25. Yang, W. Improved recursive algorithm for light scattering by a multilayered sphere. *Appl. Opt.* **42**, 1710–1720 (2003).

26. Peña, O. & Pal, U. Scattering of electromagnetic radiation by a multilayered sphere. *Comput. Phys. Commun.* **180**, 2348–2354 (2009).

27. Moridnejad, A., Preston, T. C. & Krieger, U. K. Tracking water sorption in glassy aerosol particles using morphology-dependent resonances. *J. Phys. Chem. A* **121**, 8176–8184 (2017).

28. Bastelberger, S., Krieger, U. K., Luo, B. P. & Peter, T. Time evolution of steep diffusion fronts in highly viscous aerosol particles measured with Mie resonance spectroscopy. *J. Chem. Phys.* **149**, 244506 (2018).

29. Aden, A. L. & Kerker, M. Scattering of electromagnetic waves from two concentric spheres. *J. Appl. Phys.* **22**, 1242–1246 (1951).

30. Hightower, R. L. & Richardson, C. B. Resonant Mie scattering from a layered sphere. *Appl. Opt.* **27**, 4850–4855 (1988).

31. Lock, J. A. Interference enhancement of the internal fields at structural scattering resonances of a coated sphere. *Appl. Opt.* **29**, 3180–3187 (1990).

32. Schweiger, G., Lange, S. & Kaiser, T. Structural resonances in a coated sphere: investigation of the volume-averaged source function and resonance positions. *Appl. Opt.* **33**, 7789–7797 (1994).

33. Lam, C. C., Leung, P. T. & Young, K. Explicit asymptotic formulas for the positions,

widths, and strengths of resonances in Mie scattering. *J. Opt. Soc. Am. B: Opt. Phys.* **9**, 1585–1592 (1992).

34. Teraoka, I. & Arnold, S. Theory of resonance shifts in TE and TM whispering gallery modes by nonradial perturbations for sensing applications. *J. Opt. Soc. Am. B: Opt. Phys.* **23**, 1381–1389 (2006).

35. Foreman, M. R. & Vollmer, F. Optical tracking of anomalous diffusion kinetics in polymer microspheres. *Phys. Rev. Lett.* **114**, 118001 (2015).

36. Ray, A. K. & Nandakumar, R. Simultaneous determination of size and wavelength-dependent refractive indices of thin-layered droplets from optical resonances. *Appl. Opt.* **34**, 7759–7770 (1995).

37. Kaiser, T., Roll, G. & Schweiger, G. Investigation of coated droplets in an optical trap: Raman-scattering, elastic-light-scattering, and evaporation characteristics. *Appl. Opt.* **35**, 5918–5924 (1996).

38. Stewart, D. J., Cai, C., Nayler, J., Preston, T. C., Reid, J. P., Krieger, U. K., Marcolli, C. & Zhang, Y. H. Liquid–Liquid Phase Separation in Mixed Organic/Inorganic Single Aqueous Aerosol Droplets. *J. Phys. Chem. A* **119**, 4177–4190 (2015).

39. Gorkowski, K., Beydoun, H., Aboff, M., Walker, J. S., Reid, J. P. & Sullivan, R. C. Advanced aerosol optical tweezers chamber design to facilitate phase-separation and equilibration timescale experiments on complex droplets. *Aerosol Sci. Technol.* **50**, 1327–1341 (2016).

40. Gorkowski, K., Donahue, N. M. & Sullivan, R. C. Emulsified and Liquid–Liquid Phase-Separated States of α-Pinene Secondary Organic Aerosol Determined Using Aerosol Optical Tweezers. *Environ. Sci. Technol.* **51**, 12154–12163 (2017).

41. Gorkowski, K., Donahue, N. M. & Sullivan, R. C. Emerging investigator series: determination of biphasic core–shell droplet properties using aerosol optical tweezers. *Environ. Sci. Processes Impacts* **20**, 1512–1523 (2018).

42. Ovadnevaite, J., Zuend, A., Laaksonen, A., Sanchez, K. J., Roberts, G., Ceburnis, D., Decesari, S., Rinaldi, M., Hodas, N., Facchini, M. C. *et al.* Surface tension prevails over solute effect in organic-influenced cloud droplet activation. *Nature* **546**, 637–641 (2017).

43. Liu, P., Song, M., Zhao, T., Gunthe, S. S., Ham, S., He, Y., Qin, Y. M., Gong, Z., Amorim, J. C., Bertram, A. K. *et al.* Resolving the mechanisms of hygroscopic growth and cloud condensation nuclei activity for organic particulate matter. *Nat. Commun.* **9**, 1–10 (2018).

44. Davies, J. F., Zuend, A. & Wilson, K. R. Technical note: The role of evolving surface tension in the formation of cloud droplets. *Atmos. Chem. Phys.* **19**, 2933–2946 (2019).

45. Jenkins, F. A. & White, H. E. *Fundamentals of Optics* (McGraw-Hill, New York, 1976), 4th edn.

46. Bohren, C. F. & Huffman, D. R. *Absorption and Scattering of Light by Small Particles* (Wiley-VCH, 1983).

47. Cantrell, C. D. Numerical methods for the accurate calculation of spherical Bessel functions and the location of Mie resonances. Tech. Rep., University of Texas at Dallas, Center for Applied Optics (1988).

48. Mie Resonance Shell Fitting (MRSFIT). `http://www.meteo.mcgill.ca/~tpreston/code.html`.

49. Hill, S. C., Rushforth, C. K., Benner, R. E. & Conwell, P. R. Sizing dielectric spheres and cylinders by aligning measured and computed resonance locations: algorithm for multiple orders. *Appl. Opt.* **24**, 2380–2390 (1985).

50. Daimon, M. & Masumura, A. Measurement of the refractive index of distilled water from the near-infrared region to the ultraviolet region. *Appl. Opt.* **46**, 3811–3820 (2007).

51. Miles, R. E. H., Walker, J. S., Burnham, D. R. & Reid, J. P. Retrieval of the complex refractive index of aerosol droplets from optical tweezers measurements. *Phys. Chem. Chem. Phys.* **14**, 3037–3047 (2012).

52. Abramowitz, M. & Stegun, I. A. *Handbook of mathematical functions with formulas* (Dover Publications, New York, 1965), 9th edn.